7-29-2023

Silicon-based mid infrared on-chip gas sensor using Fano resonance of coupled plasmonic microcavities

Sherif M. Sherif

Mohamed A. Swillam

Silicon-based Mid Infrared On-Chip Gas Sensor Using Fano Resonance of Coupled Plasmonic Microcavities

Sherif M. Sherif
The American University in Cairo
Mohamed A. Swillam (m.swillam@aucegypt.edu)
The American University in Cairo

Article

Keywords: Fano Resonance, Mid Infrared Sensors, Plasmonics, Microcavities, Coupled Cavities

Posted Date: September 14th, 2022

DOI: https://doi.org/10.21203/rs.3.rs-2049865/v1

Additional Declarations: No competing interests reported.

Version of Record: A version of this preprint was published at Scientific Reports on July 29th, 2023. See the published version at https://doi.org/10.1038/s41598-023-38926-9.

Abstract

Sensing in the mid infra-red spectral range is highly desirable for the detection and monitoring of different gases. We hereby propose a CMOS compatible silicon-based sensor that operates at (3.5-10 μm) within the mid infra-red range. The silicon material is doped to the level that shifts its plasmonic resonance to 3 μm wavelength. The sensor device comprises an in-line rectangular microcavity and a stub microcavity resonator. The resonance frequencies/wavelengths of the two resonators were studied with different design dimensions. When the two resonators are designed to resonate at close frequencies, the interesting Fano resonance with its distinct and sharp line shape is generated due to the interference between the two resonance profiles. Fano resonance is useful for highly sensitive measurements due to its abrupt intensity changing profile. The sensor is studied and analyzed using Finite Difference Element and 2D Finite Difference Time Domain methods. The sensor's performance is characterized by its high sensitivity of 6000 nm/RIU, FOM of 353, and limited insertion loss of 0.45 dB around 6.5 μm operation wavelength. Furthermore, we develop the sensor for simultaneously detecting methane CH4 and nitrous oxide N2O gases at 3.5 μm and 4.5 μm wavelengths, respectively.

Introduction

Mid infra-red sensing is of special importance due to its applications in different domains such as telecommunication, defense, environmental and industrial monitoring, as many gases have their absorption fingerprints in the mid infra-red range [1–2]. Optical sensors are being developed based on two main platforms: the conventional silicon Si photonic and plasmonic platforms. While Si structures have the advantages of being CMOS compatible and having low waveguiding losses, plasmonic structures can have much smaller dimensions. Moreover, plasmonics possess the interesting properties of enhancing and confining the electromagnetic fields in small regions [3–4] such as in metal-insulator-metal waveguides, plasmonic slots, and cavities. The issue with the commonly used noble metals Au and Ag is that they have a fixed density of free electrons resulting in a fixed plasmonic resonance frequency, in addition to being CMOS incompatible. On the contrary, doped semiconductors [5–6] have the advantages of CMOS compatibility, and tunability of plasmonic resonance frequency with doping concentration [7].

Sensors working principles are usually based on different configurations with strong optical resonating and interference effects such as ring resonators [8–9], and Mach Zender interferometers [10–11]. However, we would like to study the effect of coupled resonators in mid infra-red sensing which can potentially improve sensors performance. Coupling two or more resonators can lead to peculiar properties and spectral line-shapes with special profiles such as the Fano resonance [12–14], the Electromagnetically Induced Transparency, and the Borrmann effect [15].

Fano resonance is promising in sensing applications since it possesses a distinct sharp line-shape. The generation of Fano resonance is described by the interference of wide and narrow spectral lines or resonances [14], which results in a redistribution of the electromagnetic fields in the microcavities.

Different materials and designs were investigated to develop state of the art Fano resonance-based sensors operating in the mid infra-red range including graphene and Au nano-antenna arrays [16], and nanodisks [17], 1D photonic crystal structure composed of Al, Au, Ag, and Pt [18], Ag nanorods [19], Si Lucky knot structure [20], and the performance of these sensors is compared to our Fano resonance based sensor in Table 1.

In this work, we introduce a Fano resonance based mid infrared sensor which achieves 6000 nm/RIU sensitivity at the 6.5 μm wavelength, and an insertion loss of 0.45 dB. We begin our investigation by analyzing the response of an in-line rectangular cavity resonator [21] and its resonance profiles. Then we study the spectral response and the resonance orders of the stub cavity resonator. Then, we integrate the in-line and stub rectangular cavity resonators in the same device and optimize them to resonate at close frequencies and study the response of these coupled resonators. Finally, we develop the sensor for the detection of two gases on the same chip by generating two Fano resonances that correspond to the CH_4 and N_2O gases strong absorption bands in the mid infra-red at 3.5 μm and 4.5 μm [22–23].

Device Structure

A. Metal-Insulator-Metal Bus Waveguide

A doped Si wafer of thickness 220 nm on a 1 μm thick sapphire substrate is etched to form the bus waveguide of width 100 nm as shown in Fig. 1. The Si layer has a doping concentration of $5 \times 10^{20} cm^{-3}$, and its plasma resonant frequency is at 3 μm [6], thereby enabling plasmonic properties at wavelengths in the mid infrared spectral range. A commercial waveguide simulator based on the Finite Difference Eigenmode solver [24] was used to calculate the modal properties of the metal-insulator-metal bus waveguide. At an excitation wavelength of 6 μm, metallic boundary conditions, and mesh steps of 5 nm in both x and y coordinates, the plasmonic slot type waveguide is characterized by a complex effective index of 1.461 + 0.002j, and a modal loss of 0.02 dB/μm.

The mode profile |Ex| of the excited plasmonic mode is shown in Fig. 2, where the electric field is well-confined in the plasmonic slot. Moreover, we study the dispersion of the excited plasmonic mode in the mid infra-red range of 4–10 μm as shown in Fig. 3.

B. In-line Rectangular Cavity Resonator

2D-FDTD calculations were performed using an electromagnetic simulator [25] to calculate the response and analyze the performance of the proposed designs. A simulation time of 20,000 fs was sufficient to allow all fields including the cavity resonant fields to drop to zero by the end of the simulation process. An auto non-uniform mesh type was implemented which has the highest possible accuracy setting with a minimum mesh step of 0.25 nm. To minimize fields reflections back to the simulation region, 64 uniaxial anisotropic perfectly matched layers were used for the boundary conditions. The response of the in-line rectangular cavity resonator has the form of a bandpass filter [16] as shown in Fig. 4, with the spectral

band becomes wider for smaller rectangular widths due to the larger interaction of the fields with the metal boundaries.

The Quality-factor defined by ($Q = \lambda / \Delta\lambda$) where λ is the central wavelength, and $\Delta\lambda$ is the FWHM of the resonance band, is shown in Fig. 5, where the Q-factor shows a linear relation with the in-line rectangular resonator width. The length of the rectangular resonator controls the central position of the resonance band as shown in Fig. 6.

The electric field distribution within the rectangular cavity is studied at two different resonant orders as shown in Fig. 7, where strong confinement of the electric field component Ex in the rectangular cavity is observed.

C. Stub Rectangular Cavity Resonator

The stub rectangular cavity also shows distinct resonance orders but of much sharper lines as shown in Fig. 8, and higher Q-factors. The Q-factor of the 200 nm wide stub waveguide resonance line reaches 350, while that of the in-line resonator of the same width was only 3.

The stub resonator is characterized by its sharp resonances, where its wavelength positions are given by:

$$\lambda_m = \frac{2 l_{stub} n_{eff}}{m} \quad (1),$$

where l_{stub} is the stub length, n_{eff} is the plasmonic slot mode effective index, and m is the resonance order.

Fano Resonance Generation

The Fano resonance is the result of coupling a discrete localized state to a continuum of states, for example when two oscillators with strongly different damping rates with broad and narrow spectral lines are coupled together [14]. To generate the Fano resonance in our structure, we integrate the in-line and stub resonators on the same structure and optimize them “based on our studies in the previous sections” to resonate at close frequencies, such that the sharp resonance of the stub resonator couples with the decaying tail of the broader resonance of the in-line resonator as shown in Fig. 10, which shows the generation of the Fano resonance at 5.5 μm and 6.5 μm wavelengths with an insertion loss of 0.45 dB.

Figure 11 shows the electric field distribution in the resonators when the Fano resonance is generated, where it can be observed that at λ = 6 μm, at the top of the broader line, the field is stronger and confined in the in-line cavity. While at the Fano resonance position λ = 6.5 μm, the field is mainly confined in the stub resonator, while the in-line cavity possesses weaker field that corresponds to the decaying tail.

The integrated and coupled resonators structure can be used in sensing applications utilizing the sharpness and high sensitivity of the Fano resonance. The performance and spectral response of the sensor is calculated by varying the surrounding medium refractive index (Fig. 11). The calculations show

that our sensor has a sensitivity ($S = \Delta\lambda/\Delta n$) of 6000 nm/RIU, while the FOM ($FOM = S/FWHM$) is 353, and Q = 385.

A comparison between our proposed sensor and recently published Fano sensors in the mid infra-red range is demonstrated in Table 1, which shows that our sensor possesses a high sensitivity with a fairly simple design while being CMOS compatible as doped Si and not metals was used for plasmonic effects generation.

Table 1
Comparison between Fano resonance-based sensors in the mid infra-red range.

Year [Ref]	Materials	Unit Structure	λ (μm)	Sensitivity (nm/RIU)	FOM $(RIU)^{-1}$	Insertion Loss (dB)
2019 [16]	Au, and Graphene	Nano-antenna array	6.5	2300	28.75	4.5
2019 [18]	Al, Au, Ag, and Pt	1D Photonic crystal	7	5018	1477.5	NA
2020 [19]	Ag	Stub, and nanorods	3	5140	NA	0.96
2020 [17]	Au, and Graphene	nanodisks	10	7930	158.7	2.2
2021 [20]	Si	Lucky knot	7	986	32.7	NA
This work	Doped Si	Stub	6.5	6000	353	0.45

Simultaneous-gas Sensing In The Mid Infra-red Spectral Range

The sensor operation was further developed to achieve simultaneous sensing by integrating the in-line microcavity with two resonant stub microcavities. The in-line cavity provides the wide spectrum centered at 3.8 μm, while the stub cavities resonate at 3.5 μm and 4.5 μm which correspond to the strong absorption bands of CH_4 and N_2O gases, respectively [22–23], as shown in Fig. 13.

Fabrication Tolerance

Different etching methods are typically used for etching Si wafers after photolithography or electron beam lithography [25–26], such as reactive ion etching [27], and inductively coupled plasma dry etching [28–29]. Hereby, due to its high resolution, we recommend using e-beam lithography to define the metal-insulator-metal waveguide, the rectangular resonator, and the stub resonator. The stub microcavity is obviously less fabrication tolerant than the larger rectangular cavity, so we study the fabrication tolerance of the stub microcavity in Fig. 14, where its dimensions were changed by ± 50 nm. While studying the resonators response with the changes in the stub width, it was noticed that the Fano resonance is no

longer recognizable for larger widths due to the domination of the wide resonance line of the rectangular cavity, so we limit Fig. 14b to widths with − 50 nm fabrication errors.

Conclusion

A mid infra-red gas sensor was demonstrated and studied. The sensor is composed of a doped Si layer that was etched to form a plasmonic slot waveguide, in-line, and stub cavity resonators. The doping level used pushes the plasmonic resonance of the Si to 3 mm, which results in exhibiting plasmonic properties in the mid infra-red range. The performance of each resonator type was investigated individually and then they were both integrated together. When coupled at close frequencies, Fano resonance was generated because of the interference between the wide response of the in-line microcavity and the sharper resonance of the stub resonator. Performance parameters were measured such as the sensitivity, FOM and insertion loss of the device.

Declarations

Author contribution

S. M. Sherif proposed the idea and design, and M. A. Swillam developed the concept and defined the functionality and applications. S. M. Sherif performed the numerical simulations and wrote the paper draft. M. A. Swillam revised and modified the manuscript. All authors discussed, revised, edited, and approved the manuscript.

Competing interests

The authors declare no competing interests. Additional information Correspondence and requests for materials should be addressed to M.A.S. Reprints and permissions information is available at www.nature.com/reprints. Publisher's note Springer Nature remains neutral with regard to jurisdictional claims in published maps and institutional affiliations.

References

1. F. K. Tittel, D. Richter, and A. Fried, "Mid-infrared laser applications in spectroscopy," in Solid-State Mid-Infrared Laser Sources, I. T. Sorokina and K. L. Vodopyanov, Ed., pp. 458– 529, Springer, Berlin Heidelberg (2003).
2. S. Law et al., "All-semiconductor plasmonic nanoantennas for infrared sensing," Nano Lett. 13(9), 4569–4574 (2013).
3. S. A. Maier and H. A. Atwater, "Plasmonics: localization and guiding of electromagnetic energy in metal/dielectric structures," J. Appl. Phys. 98(1), 011101 (2005).
4. D. K. Gramotnev, and S.I. Bozhevolnyi, 2010. Plasmonics beyond the diffraction limit. Nature photonics, 4(2), pp.83–91.

5. Sherif, S.M. and Swillam, M.A., 2016. Metal-less silicon plasmonic mid-infrared gas sensor. Journal of Nanophotonics, 10(2), p.026025.
6. R. Gamal, Y. Ismail, and M. A. Swillam, “Silicon waveguides at the mid-infrared,” J. Lightwave Technol. 33(15), 3207–3214 (2015).
7. R. Soref, R. E. Peale, and W. Buchwald, “Longwave plasmonics on doped silicon and silicides,” Opt. Express 16(9), 6507–6514 (2008).
8. Sherif, S.M., Elsayed, M.Y., Shahada, L.A. and Swillam, M.A., 2019. Vertical silicon nanowire-based racetrack resonator optical sensor. Applied Physics A, 125(11), pp.1–6.
9. Shafaay, S. and Swillam, M.A., 2019. Integrated slotted ring resonator at mid-infrared for on-chip sensing applications. Journal of Nanophotonics, 13(3), p.036016.
10. El Shamy, R.S., Swillam, M.A., ElRayany, M.M., Sultan, A. and Li, X., 2022, January. Compact Gas Sensor Using Silicon-on-Insulator Loop-Terminated Mach–Zehnder Interferometer. In Photonics (Vol. 9, No. 1, p. 8). Multidisciplinary Digital Publishing Institute.
11. El Shamy, R.S., Khalil, D. and Swillam, M.A., 2020. Mid infrared optical gas sensor using plasmonic Mach-Zehnder interferometer. Scientific reports, 10(1), pp.1–9.
12. Rahmani, M., Luk'yanchuk, B. and Hong, M., 2013. Fano resonance in novel plasmonic nanostructures. Laser & Photonics Reviews, 7(3), pp.329–349.
13. Miroshnichenko, A.E., Flach, S. and Kivshar, Y.S., 2010. Fano resonances in nanoscale structures. Reviews of Modern Physics, 82(3), p.2257.
14. Limonov, M.F., Rybin, M.V., Poddubny, A.N. and Kivshar, Y.S., 2017. Fano resonances in photonics. Nature Photonics, 11(9), pp.543–554.
15. Sherif, S.M., Zografopoulos, D.C., Shahada, L.A., Beccherelli, R. and Swillam, M., 2017. Integrated plasmonic refractometric sensor using Fano resonance. Journal of Physics D: Applied Physics, 50(5), p.055104.
16. Hong, Q., Luo, J., Wen, C., Zhang, J., Zhu, Z., Qin, S. and Yuan, X., 2019. Hybrid metal-graphene plasmonic sensor for multi-spectral sensing in both near-and mid-infrared ranges. Optics Express, 27(24), pp.35914–35924.
17. Zhang, J., Hong, Q., Zou, J., He, Y., Yuan, X., Zhu, Z. and Qin, S., 2020. Fano-resonance in hybrid metal-graphene metamaterial and its application as mid-infrared plasmonic sensor. Micromachines, 11(3), p.268.
18. Ahmed, A.M. and Mehaney, A., 2019. Ultra-high sensitive 1D porous silicon photonic crystal sensor based on the coupling of Tamm/Fano resonances in the mid-infrared region. Scientific reports, 9(1), pp.1–9.
19. Chau, Y.F.C., 2020. Mid-infrared sensing properties of a plasmonic metal–insulator–metal waveguide with a single stub including defects. Journal of Physics D: Applied Physics, 53(11), p.115401.
20. Zhang, Y., Liang, Z., Meng, D., Qin, Z., Fan, Y., Shi, X., Smith, D.R. and Hou, E., 2021. All-dielectric refractive index sensor based on Fano resonance with high sensitivity in the mid-infrared region.

Results in Physics, 24, p.104129.

21. Kotb, R., Ismail, Y. and Swillam, M.A., 2013. Integrated metal-insulator-metal plasmonic nano resonator: an analytical approach. Progress In Electromagnetics Research Letters, 43, pp.83–94.
22. Jin, T., Zhou, J., Wang, Z., Gutierrez-Osuna, R., Ahn, C., Hwang, W., Park, K. and Lin, P.T., 2018. Real-time gas mixture analysis using mid-infrared membrane microcavities. Analytical chemistry, 90(7), pp.4348–4353.
23. Tittel, F.K., Lewicki, R., Lascola, R. and McWhorter, S., 2013. Emerging infrared laser absorption spectroscopic techniques for gas analysis. Trace analysis of specialty and electronic gases, pp.71–109.
24. Lumerical Inc. https://www.lumerical.com/products/mode/
25. Lumerical Inc. https://www.lumerical.com/products/FDTD/
26. Kato, K., Liu, Y., Murakami, S., Morita, Y. and Mori, T., 2021. Electron beam lithography with negative tone resist for highly integrated silicon quantum bits. Nanotechnology, 32(48), p.485301.
27. Doll, P.W., Al-Ahmad, A., Bacher, A., Muslija, A., Thelen, R., Hahn, L., Ahrens, R., Spindler, B. and Guber, A.E., 2019. Fabrication of silicon nanopillar arrays by electron beam lithography and reactive ion etching for advanced bacterial adhesion studies. Materials Research Express, 6(6), p.065402.
28. Huff, M., 2021. Recent advances in reactive ion etching and applications of high-aspect-ratio microfabrication. Micromachines, 12(8), p.991.
29. Goodyear, A.L., Mackenzie, S., Olynick, D.L. and Anderson, E.H., 2000. High resolution inductively coupled plasma etching of 30 nm lines and spaces in tungsten and silicon. Journal of Vacuum Science & Technology B: Microelectronics and Nanometer Structures Processing, Measurement, and Phenomena, 18(6), pp.3471–3475.a

Figures

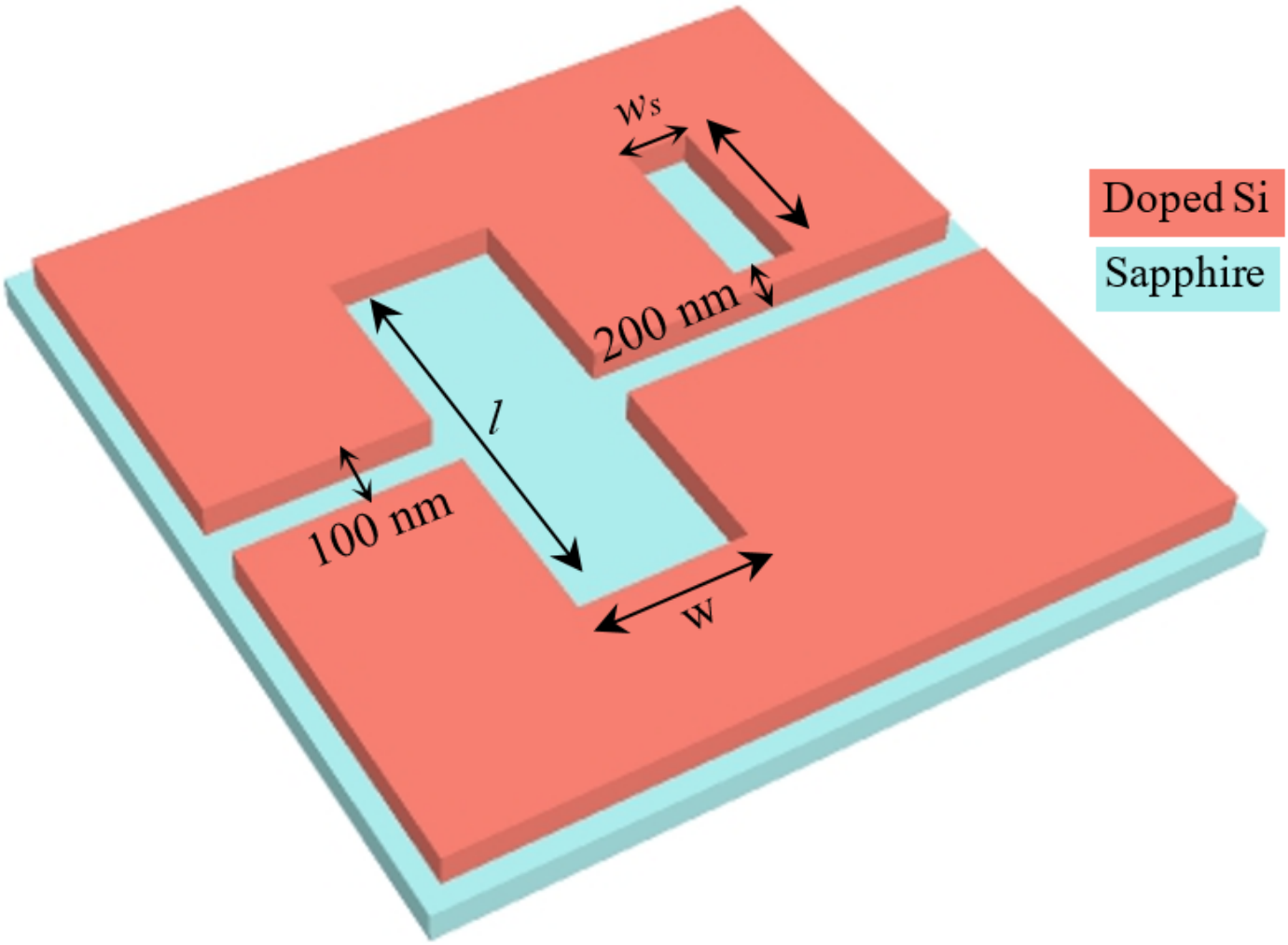

Figure 1

3D schematic of the Fano resonance-based sensor.

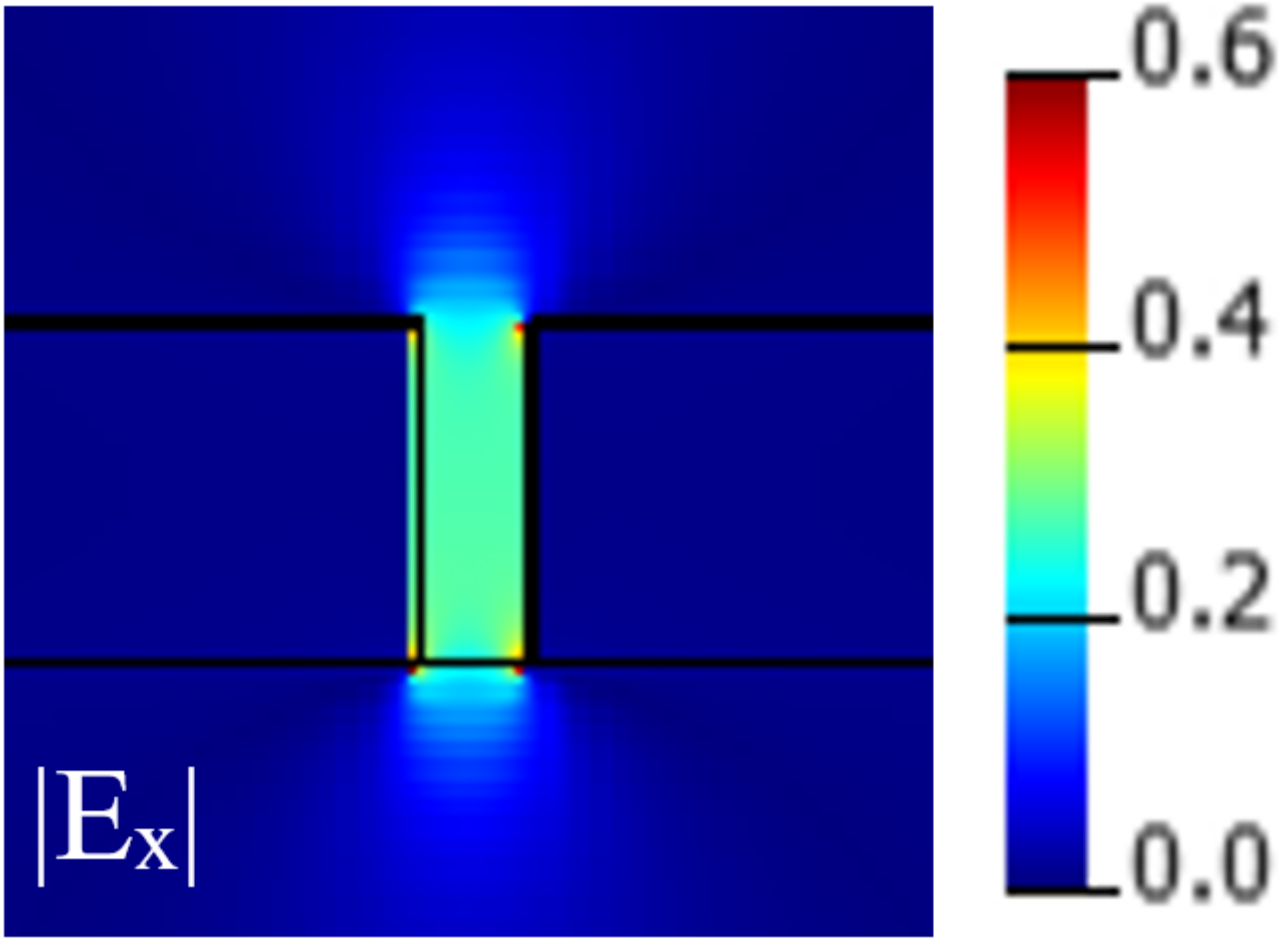

Figure 2

Plasmonic slot effective mode profile |Ex|.

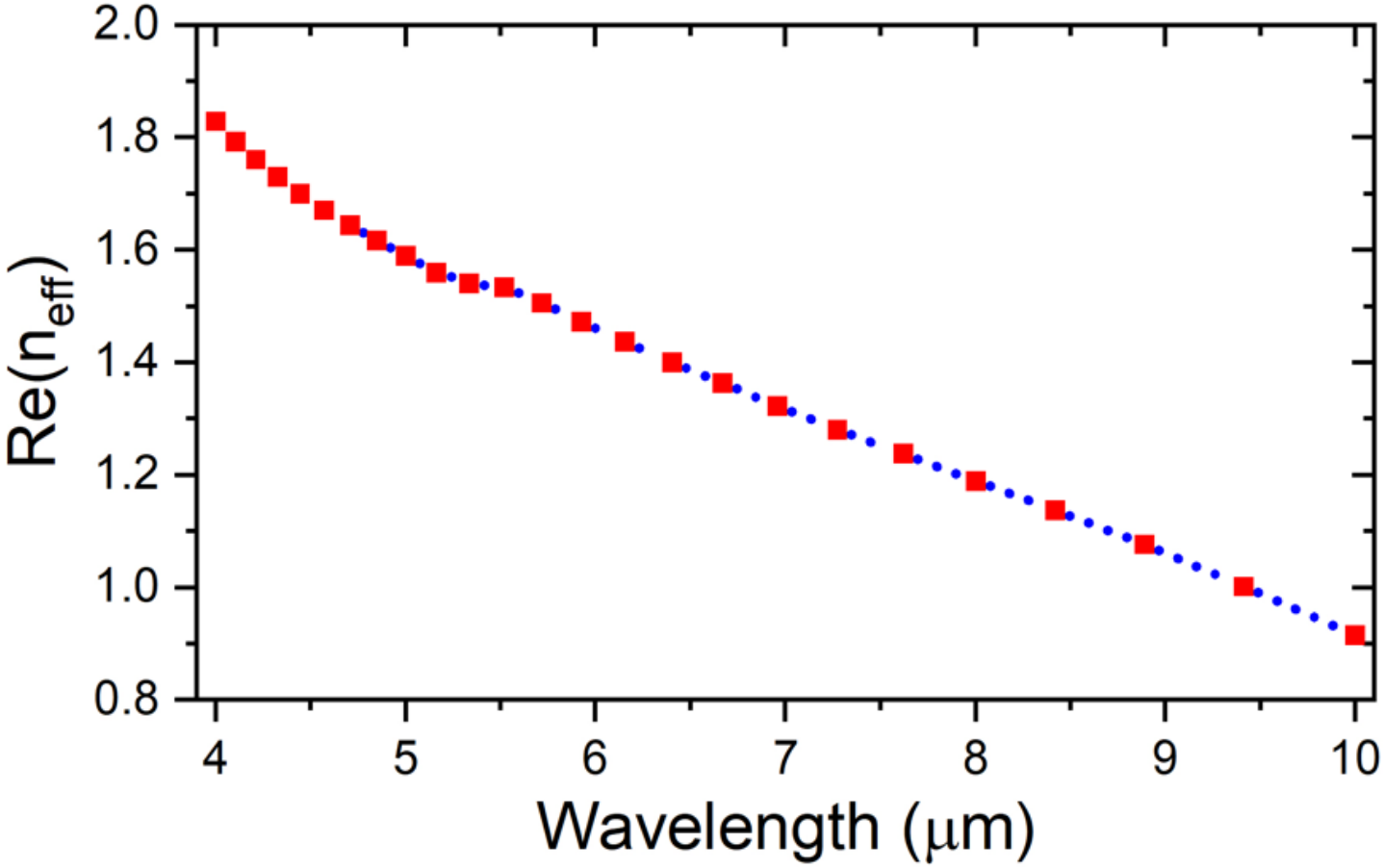

Figure 3

Excited plasmonic mode dispersion curve.

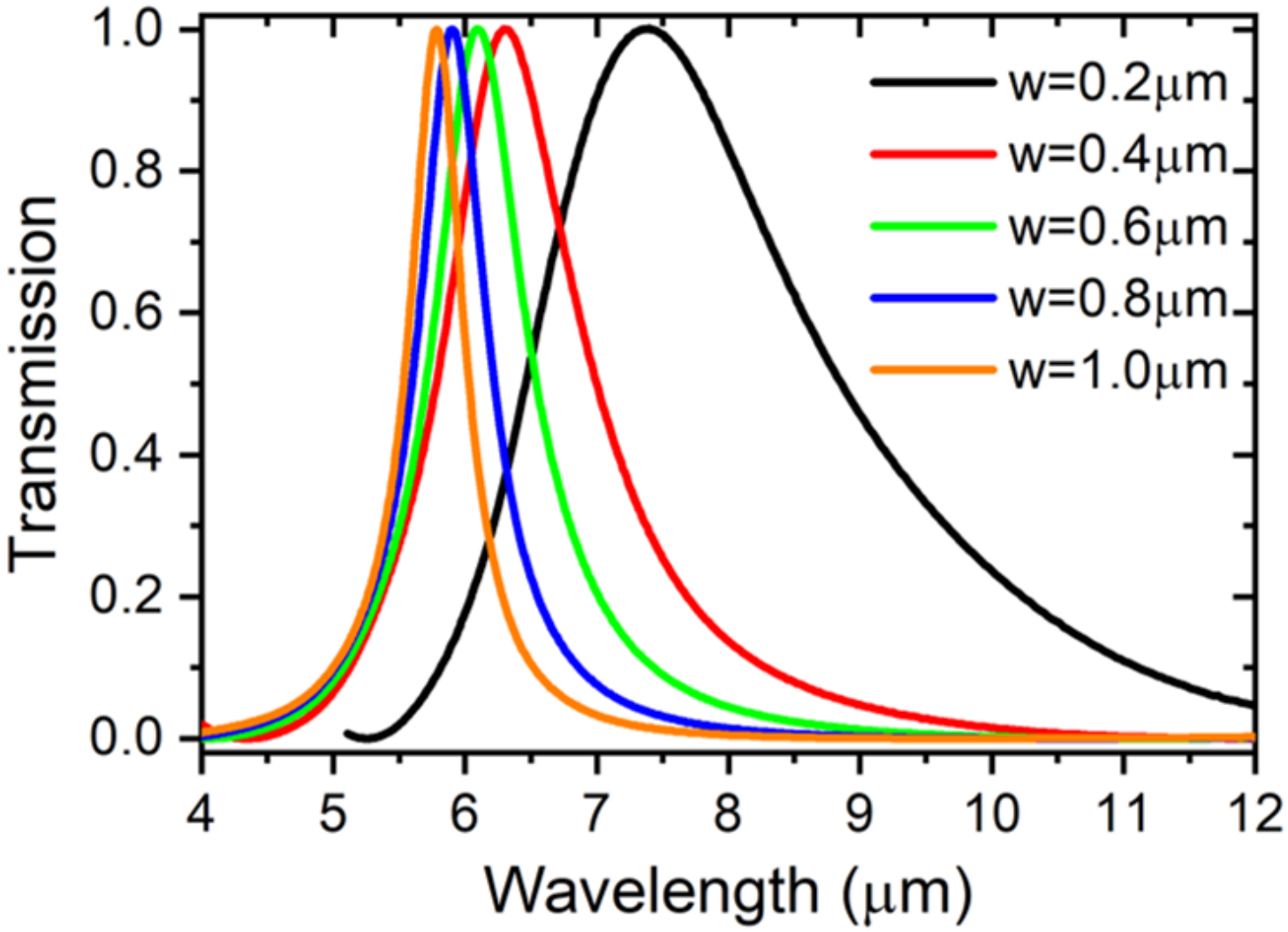

Figure 4

In-line rectangular cavity band bass filter response, l=5 μm.

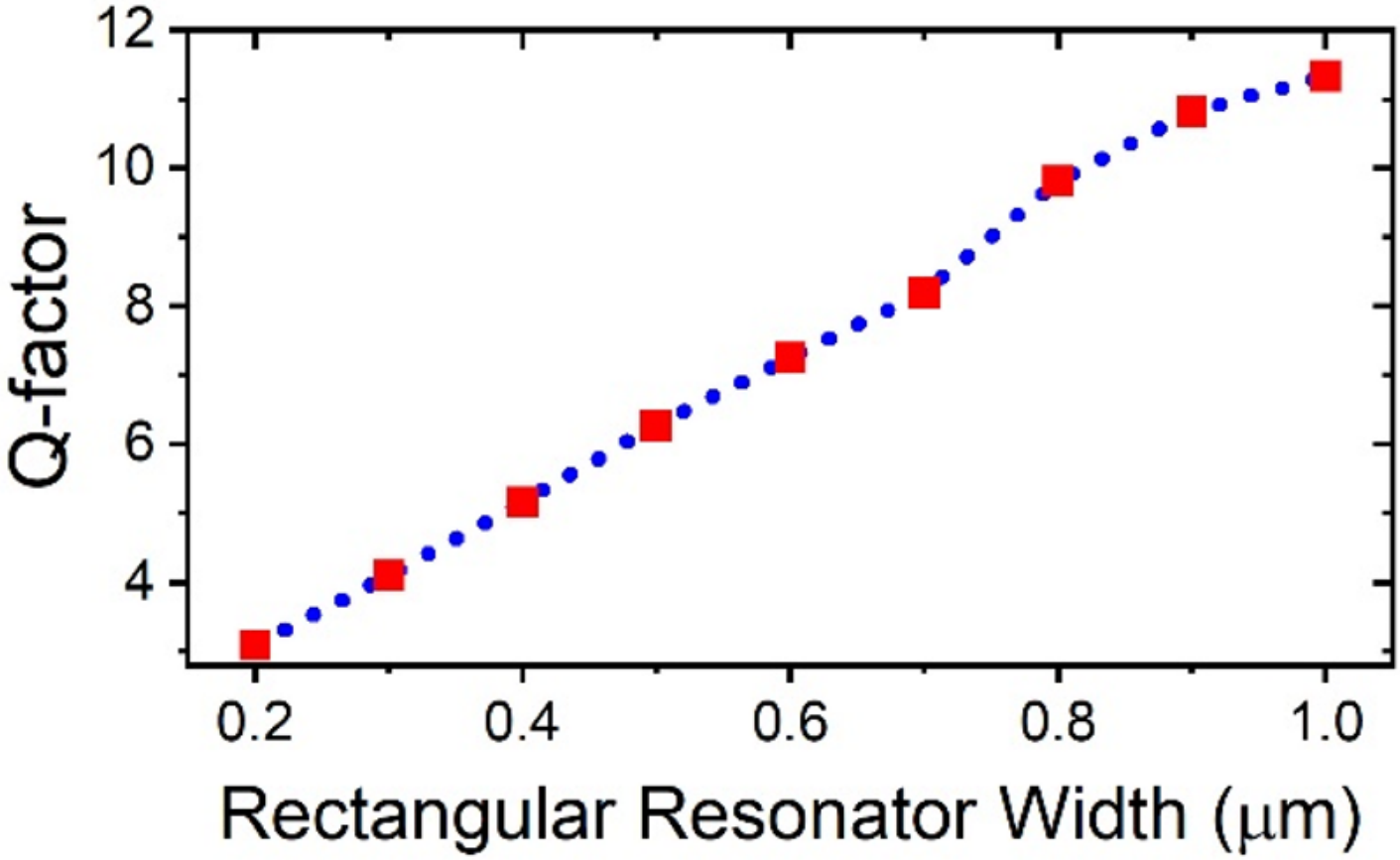

Figure 5

Resonance Q-factor with in-line cavity width.

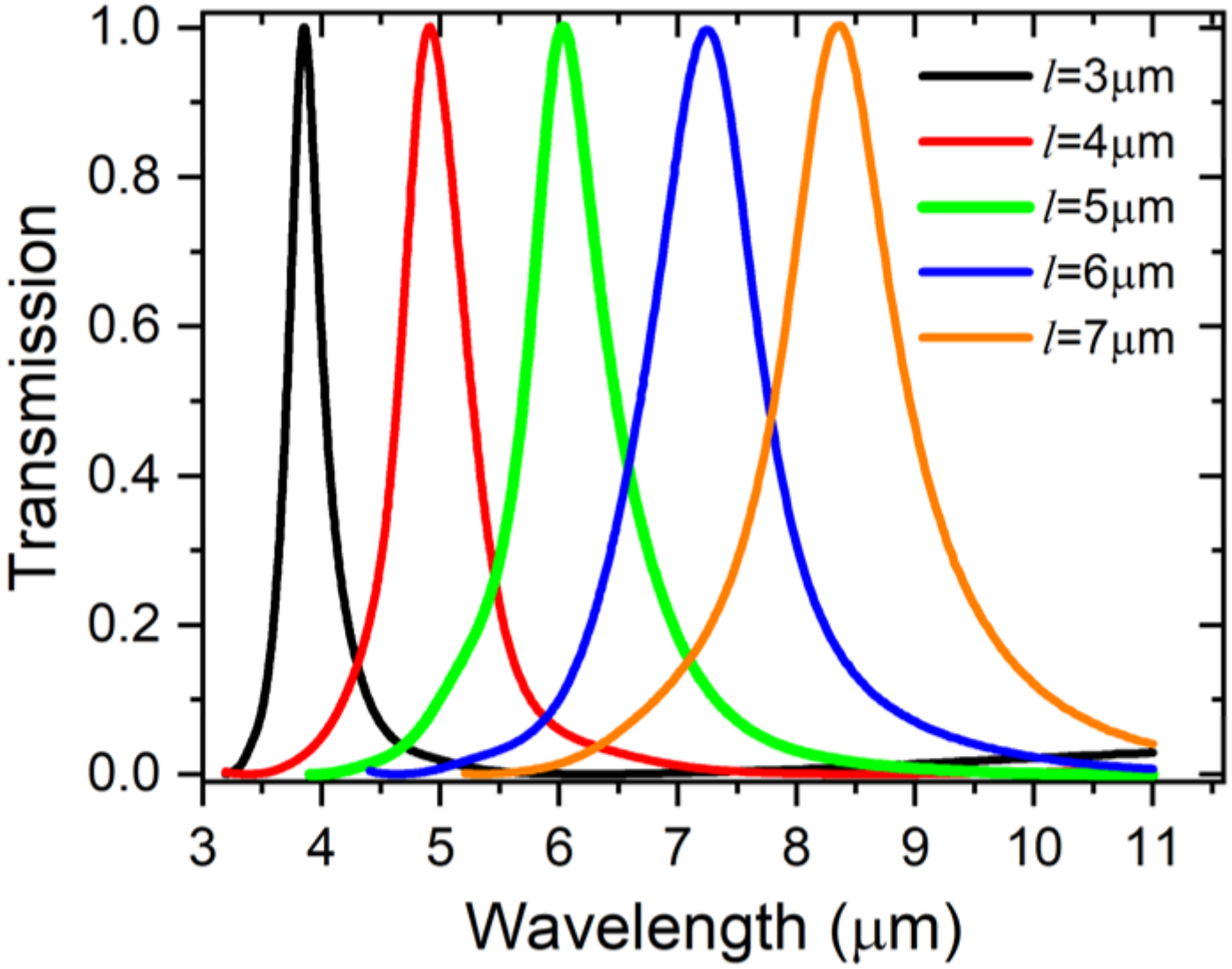

Figure 6

Resonance wavelength shift with in-line cavity length, w=0.7 μm.

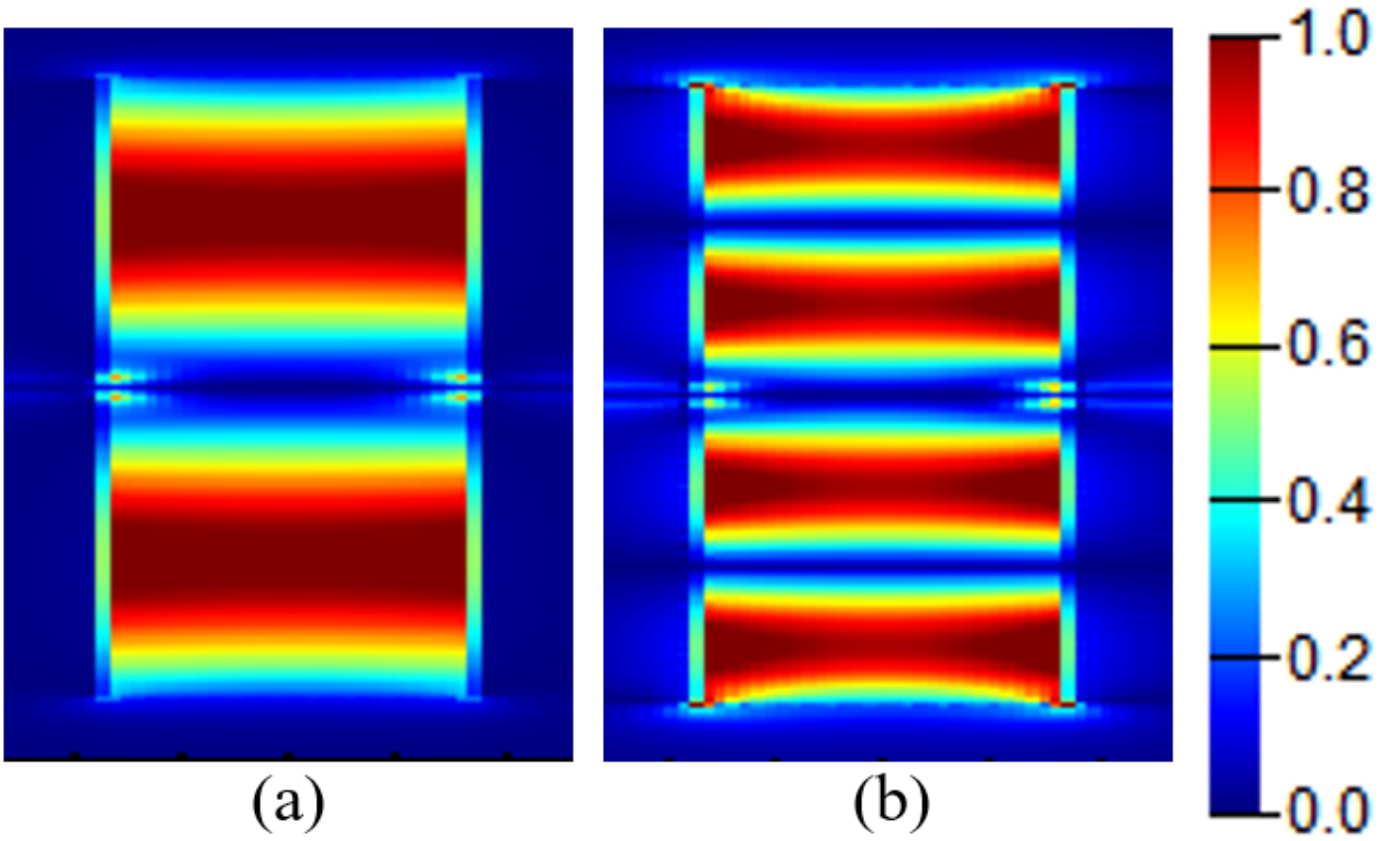

Figure 7

Electric field |Ex| distribution showing two different resonance orders in the in-line resonant cavity at (a) λ=6μm, and (b) λ =3.3 μm.

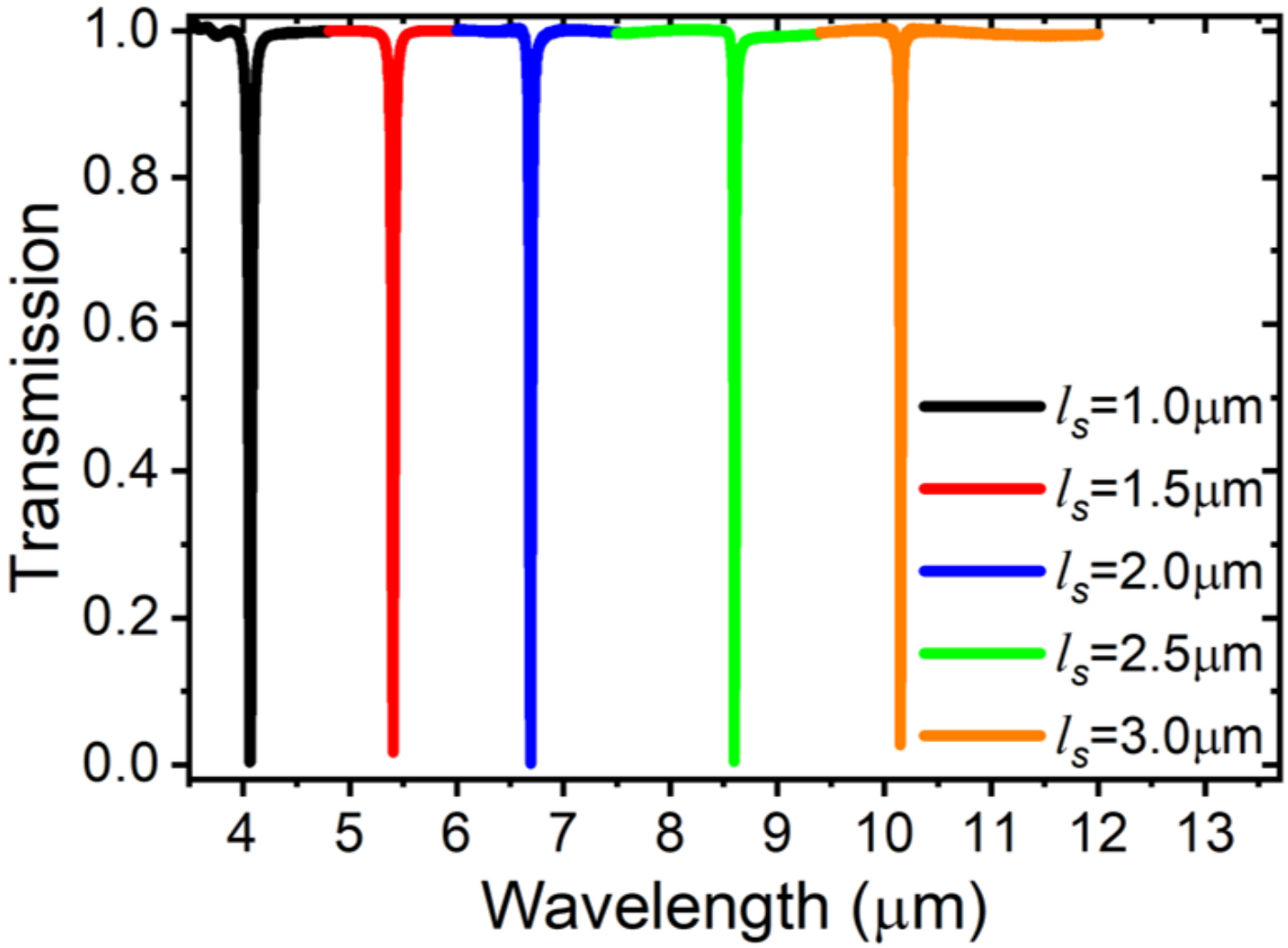

Figure 8

Stub rectangular cavity sharp resonances, ws=200 nm.

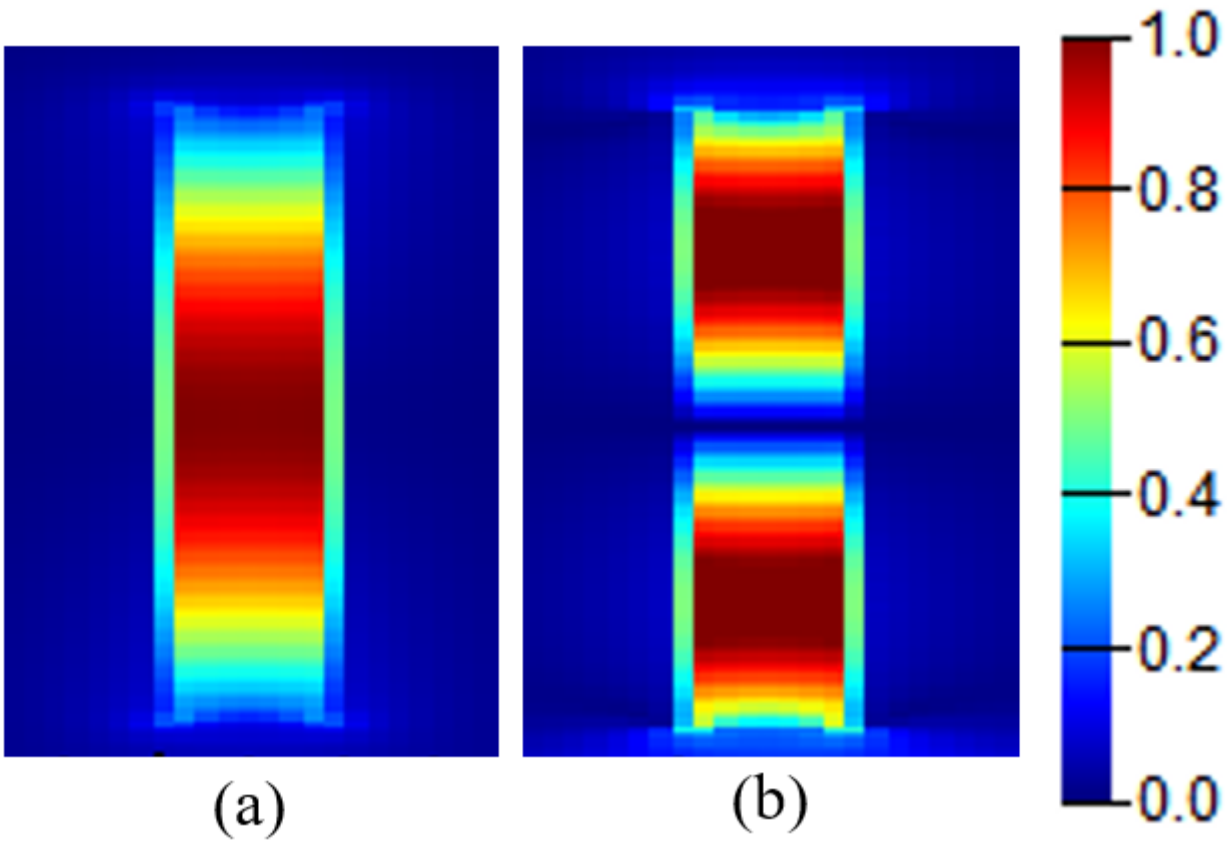

Figure 9

Electric field |Ex| distribution showing the first two resonant orders in the stub resonant cavity at (a) λ =7.1 μm, and (b) λ =3.95 μm.

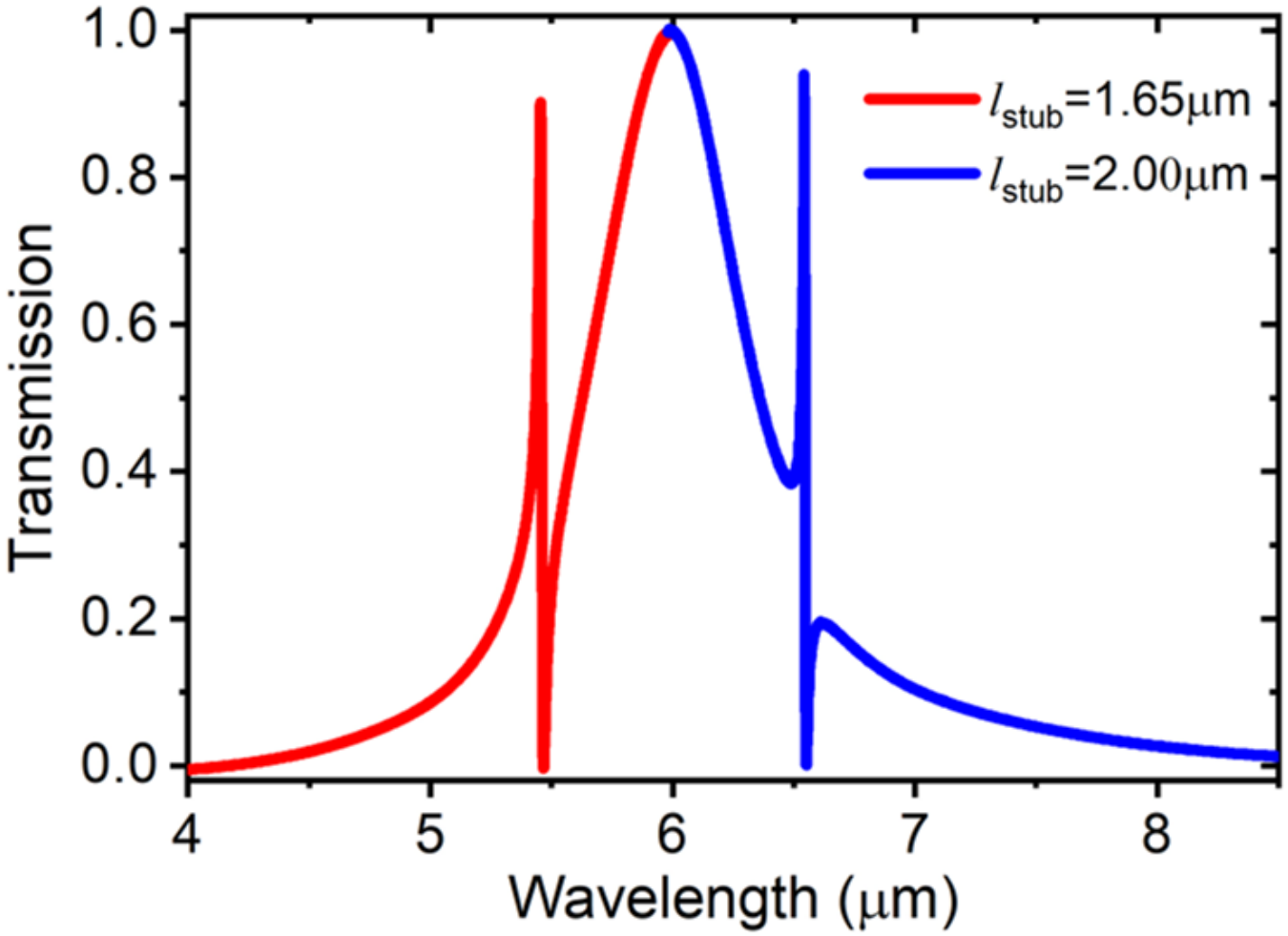

Figure 10

Fano resonance generated at two different spectral positions in response of coupling the in-line resonator and the stub resonator at close frequencies.

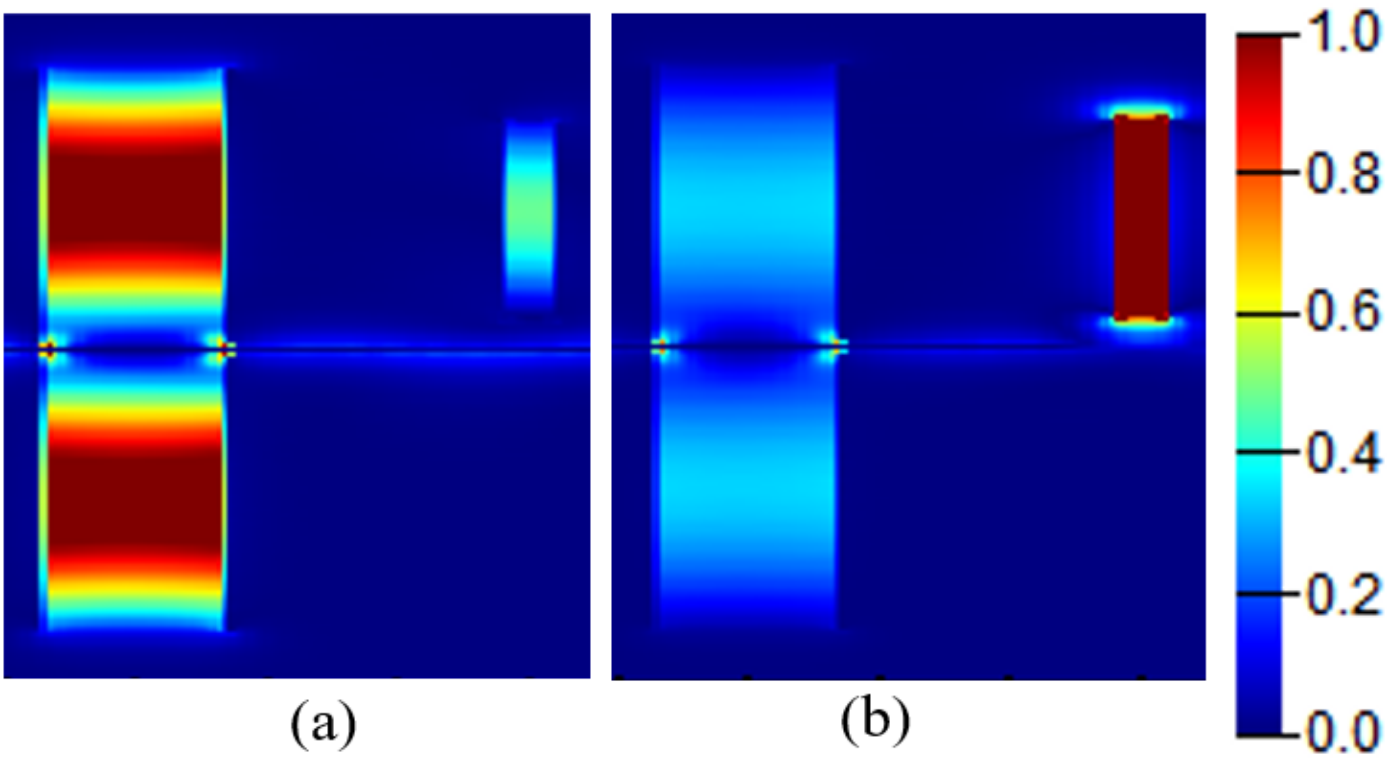

Figure 11

Electric field |Ex| distribution within the in-line and stub resonators at the Fano resonance wavelength at (a) λ=6μm, and (b) λ=6.5 μm.

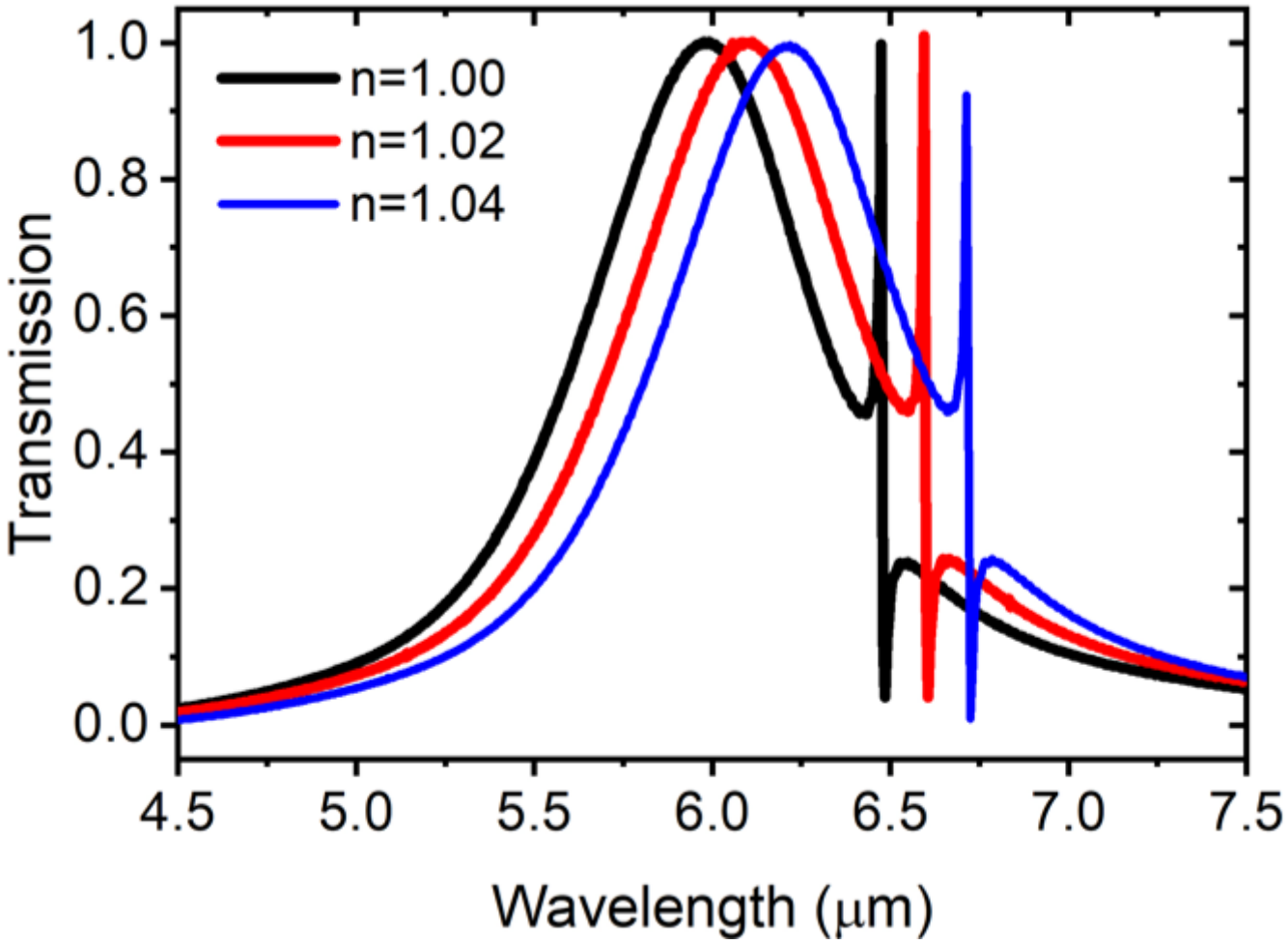

Figure 12

Fano resonance redshift with increasing surrounding gas index.

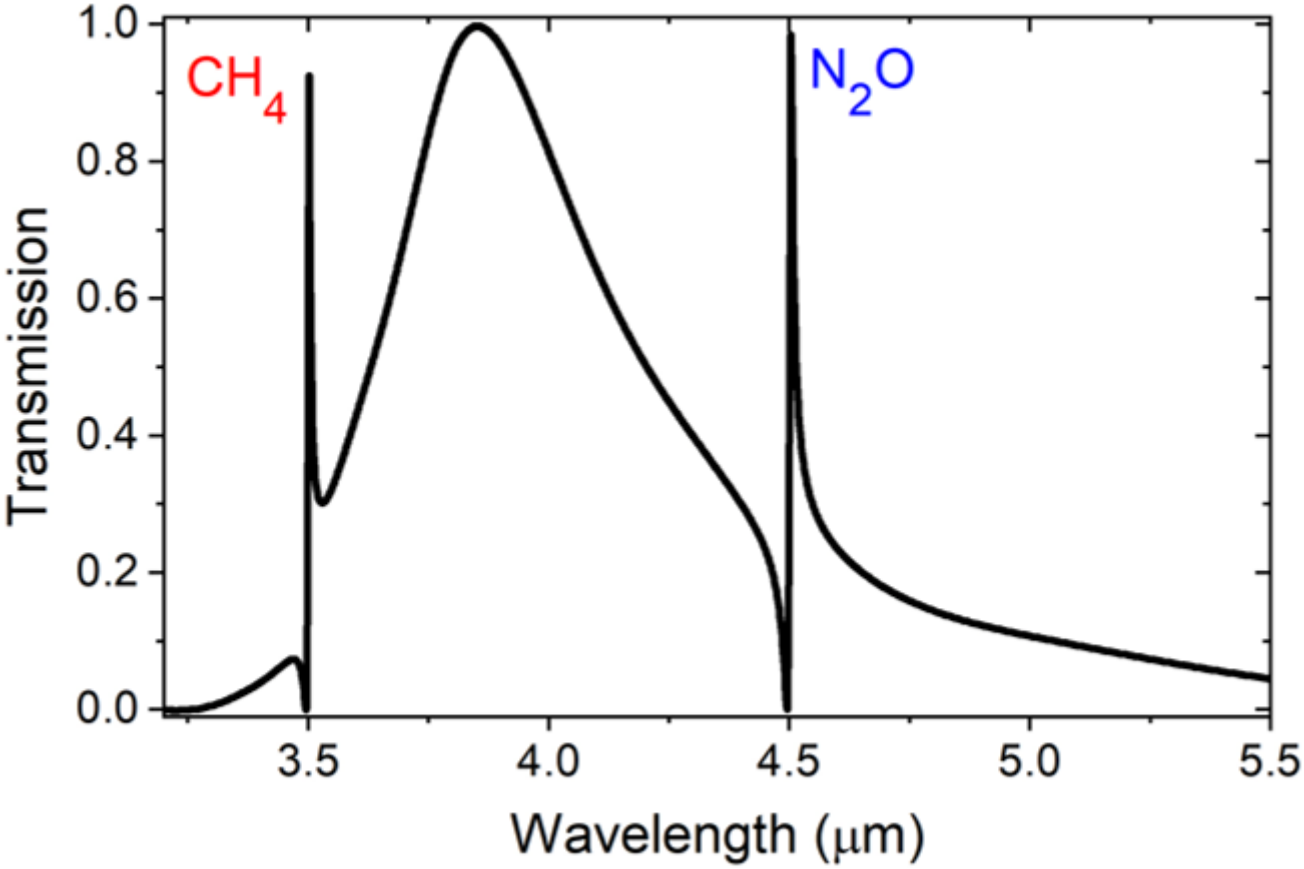

Figure 13

Detection of CH_4 and NO_2 at 3.5 μm and 4.5 μm, respectively.

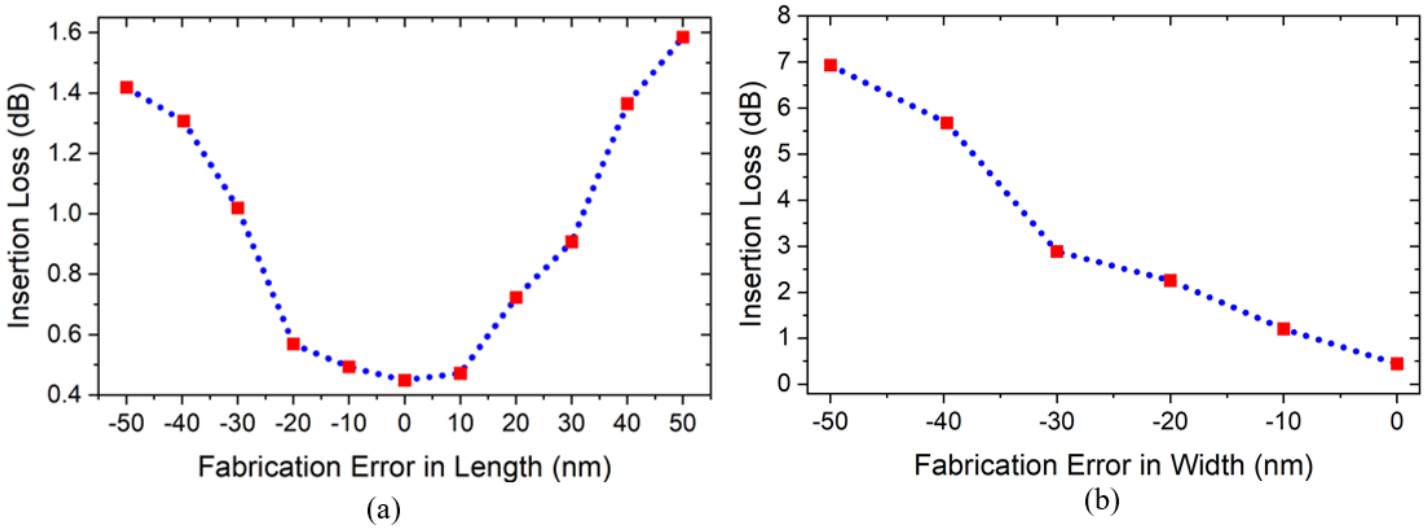

Figure 14

Fabrication tolerance represented by insertion loss measurements with the fabrication errors in length (a) and width (b) of the stub microcavity.